Ocean Modelling 81 (2014) 78–88

Contents lists available at ScienceDirect

Ocean Modelling

journal homepage: www.elsevier.com/locate/ocemod

Extreme wave parameters under North Atlantic extratropical cyclones

S. Ponce de León *, C. Guedes Soares

Centre for Marine Technology and Engineering (CENTEC), Instituto Superior Técnico, Universidade de Lisboa, Pav. Central, Av. Rovisco Pais, 1049-001 Lisboa, Portugal

ARTICLE INFO

Article history:
Received 9 September 2013
Received in revised form 14 July 2014
Accepted 21 July 2014
Available online 5 August 2014

Keywords:
Freak waves
Benjamin–Feir index
Extratropical cyclones
Wind waves
WAM
North Atlantic

ABSTRACT

A characterization of extreme wave parameters during extratropical cyclones in the Northern hemisphere is made from WAM wave model hindcasts. In February 2007 two extratropical storms were observed in the North Atlantic and the wave fields associated with them are modeled in this paper. Wave buoy and satellite altimetry data were used to validate the WAM hindcast results. The distribution of the Benjamin–Feir index (BFI), kurtosis and the ratio of maximum wave height to significant wave height (abnormality index) around the eye of the two extratropical cyclones is studied. It is found that under these conditions the BFI and kurtosis are significantly larger mainly in the fourth quadrant and also when the wind direction is aligned with the wave propagation direction. In these regions the probability of occurrence of abnormal waves is higher.

1. Introduction

Extreme waves occurring in the ocean and closed seas are dangerous to human activities and personal safety. Despite the scarcity of these events, they can be associated with severe consequences such as considerable damages to ships, offshore structures and potential loss of human life (Faulkner and Buckley, 1997; Guedes Soares et al., 2008). In a sea state described by linear theory, the probability distribution of wave heights follows a Rayleigh distribution (Longuet-Higgins, 1952). However, full scale data (Guedes Soares et al., 2011) and experiments (Onorato et al., 2004; Cherneva et al., 2009) have shown that when extreme sea states are more expectable the statistics of large wave heights do not follow this distribution and nonlinearity plays a role. In fact, several studies have shown that in some cases the Rayleigh distribution tends to under predict the actual observed heights (Longuet-Higgins, 1980; Goda, 2000; Tayfun and Fedele, 2007; among others) and alternatives on the Rayleigh distribution have been proposed in order to improve its accuracy for large waves. Comparisons with empirical data by Forristall (1984), Petrova and Guedes Soares (2011), Casas-Prat and Holthuijsen (2010) and Alkhalidi (2012), among others have reached the general conclusion that the asymptotic distributions of Tayfun (1990) and Boccotti (1981, 1989, 2000) appear to be the most accurate ones in predicting large wave heights. Later, Alkhalidi and Tayfun (2013) found a generalized model that describes large wave heights well and noticeably better than the original Boccotti distribution and other models proposed for describing wave heights affected by third-order nonlinearities.

Abnormal, rogue or freak waves are transient very high waves in relation to the sea state in which they occur, which started being identified when the abnormality index, (Dean, 1990), i.e. the ratio of maximum wave height (H) to significant wave height (Hs) would be larger than two ($H/\mathrm{Hs} > 2$). Additional conditions have been proposed by various authors as reviewed by Kharif et al. (2008), but that condition has remained as the common one. Abnormal wave occurrences have been reported from field observations in the Sea of Japan (Yasuda and Mori, 1997), the North Sea (Guedes Soares et al., 2003) and in a hurricane in the Gulf of Mexico (Guedes Soares et al., 2004; Veltcheva and Guedes Soares, 2012).

Several physical mechanisms have been suggested as responsible for the formation of these extreme waves: linear superposition of waves or spatial–temporal focusing (Kharif and Pelinovsky, 2003), interaction of waves with currents (Lavrenov, 1998), modulational instability (Benjamin–Feir instability) in crossing seas (Trulsen and Dysthe, 1997). The nonlinear enhancement of freak wave generation was explained in terms of the number of waves in a time series and the surface elevation kurtosis by Mori and Janssen (2006). This enhancement occurs with finite kurtosis (for a Gaussian time series kurtosis is zero) and can reach a three-fold increase in the ratio of freak wave occurrence. Kurtosis is a fourth-order moment of a probability density function and is related to third order nonlinear interactions (Longuet-Higgins et al., 1963). Based on the probability of occurrence calculations from North

* Corresponding author.
E-mail address: sonia.poncedeleon@centec.tecnico.ulisboa.pt (S. Ponce de León).

http://dx.doi.org/10.1016/j.ocemod.2014.07.005
1463-5003/

Sea wave measurements it was shown that the kurtosis coefficient can be used as an indicator for the occurrences of abnormal waves (Guedes Soares et al., 2011).

Directional dispersion influences the evolution of kurtosis in deep water and a decrease of kurtosis was found for directional sea states in numerical and experimental settings (Gramstad and Trulsen, 2007; Waseda, 2006; Onorato et al., 2009). Mori et al. (2011) then studied the dependence of kurtosis on the BFI and directional spread in directional sea states.

The relationship between the probability of occurrence of abnormal waves and BFI and kurtosis gives spectral wave models like WAM the opportunity of being applied for forecasting sea states with high probability of occurrence of abnormal waves.

Despite of the latest advances on the subject little information has been published about extreme waves generated under realistic conditions of extratropical storms. Young (2006) provided a directional spectrum description under hurricane conditions based on cyclones records. He showed that for almost all quadrants of the storms the dominant waves are remotely generated swell and that nonlinear wave–wave interactions play a major role in the spectral balance. Later, the abnormal waves generated under idealized typhoon conditions were examined in Mori (2012). From his work it was concluded that freak waves have a greater potential of occurring in the fourth quadrant of the typhoon.

The present work intends to gain insight about the extratropical cyclones conditions which allowed for the generation of extreme waves by using a spectral wave model. The paper is structured as follows. Section 2 is devoted to the data and methods giving different details about the wave measurements (buoys and satellite altimetry), a description about the wind forcings used. The WAM model description and wave model set up configuration are presented in Section 3. The considered extratropical cyclones are briefly described in Section 4. This is followed by the validation of the hindcast in Section 5. Section 6 presents the results and discussions focused on the spatial–temporal distributions of the main extreme wave parameters and the wave spectra characteristics in the cyclone area. General conclusions of the work were provided in Section 7.

2. Data and methods

2.1. Wave measurements

The wave hindcast was validated against two moored wave buoys data (Fig. 1) from UK Metoffice which are distributed by the JCOMM-Joint Technical Commission for Oceanography and Marine Meteorology Project (Bidlot, 2012). These moorings consist of directional wave buoys Fugro Oceanor Seawatch transmitting hourly data on the standard suite of meteorological parameters.

For the assessment of the WAM hindcast, altimetry data (JASON1) from GLOBWAVE (Ash et al., 2012) were used. The GLOBWAVE data set is homogenized with a high quality control which allows making use of these data with a spatial coverage that is ideal for a wave hindcast validation. For JASON1 the calibrations are taken from Durrant et al. (2009).

The WAM significant wave height (Hs) was compared against the GLOBWAVE L2P data (Ash et al., 2012). The GLOBWAVE data employed suitable quality control and calibration of the data streams from the various missions as described in Queffeulou and Croize-Fillon (2012). Only the calibrated Hs data flagged as “probably good measurement” were used in the present study. The method employed to filter these data is the following: WAM model results are interpolated linearly to the position and time of the satellite observations.

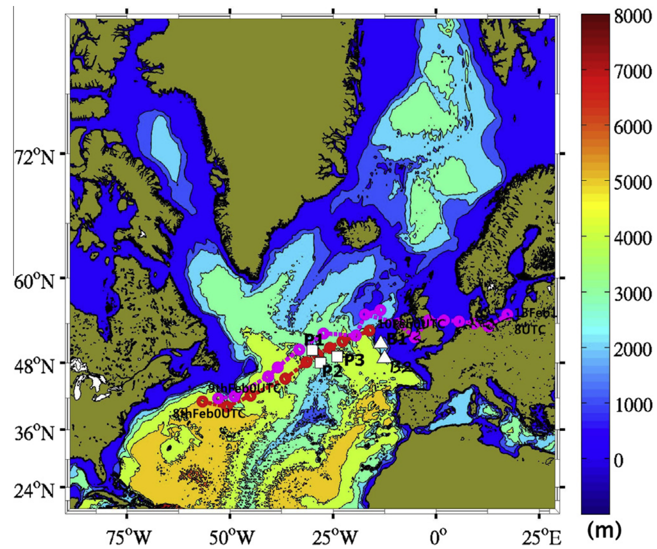

Fig. 1. Study region and the WAM model bathymetry grid (depth in meters). P1, P2, P3 – WAM output locations (white squares); B1, B2-wave buoys locations (white triangles). The cyclones tracks: 1st cyclone (red dashed line); 2nd cyclone (magenta dashed line). (For interpretation of the references to colour in this figure legend, the reader is referred to the web version of this article.)

2.2. Wind forcing

The reanalysis used for this study come from the Climate Forecast System Reanalysis (CFSR) from NOAA (Saha Suranjana et al., 2010). The CFSR is a third generation reanalysis product. It is a global, high resolution, coupled atmosphere–ocean–land surface–sea ice system designed to provide the best estimate of the state of these coupled domains over a time period. The CFSR includes coupling of atmosphere and ocean during the generation of the 6 h guess field, an interactive sea-ice model, and assimilation of satellite radiances. The CFSR global atmosphere resolution is about 38 km with 64 levels. The global ocean is 0.25° at the equator, extending to a global 0.5° beyond the tropics, with 40 levels. It is also coupled to an ocean circulation model (as opposed to using a prescribed Sea Surface Temperature (SST) over the ocean as was done earlier).

The subset of ds093.1 – NCEP Climate Forecast System Reanalysis (CFSR) selected hourly time-series products was used, with a temporal resolution of 1 h, coverage from January 1979 to December 2010 and the two spatial resolution products: 0.5° and 0.31°. For further details about this data base a complete validation of a thirty year wave hindcast using the CFSR winds can be found in Chawla et al. (2013).

2.3. Methods

The BFI and kurtosis fields obtained from the hindcast were linearly interpolated to a latitude–longitude grid centred at the cyclone’s centre position. The position of the cyclone’s centre was obtained from the NSIDC’s (National Snow and Ice Data Center) database of northern hemisphere cyclone location and characteristics (Serreze, 2009). This data set contains half-a-century of daily extratropical cyclone statistics, such as centre location and sea level pressure (SLP). Cyclone locations and characteristics were obtained by applying the updated Serreze et al. (1997) algorithm to daily Sea Level Pressure data at six hour intervals (Serreze and Barrett, 2008). The SLP source data are part of the National Centers for Environmental Prediction (NCEP) and National Center for Atmospheric Research (NCAR) Reanalysis data set.

3. The wave model

In this work the version of the WAM wave model code used is the Cy38r1, which is distributed by the ECMWF (European Centre for Medium-Range Weather Forecasts). The WAM model is formulated in terms of the frequency-direction spectrum $E(\omega,\theta)$ of the variance of the surface elevation (Janssen and Bidlot, 2009). In this version of WAM a variant of the growth limiter of Hersbach and Janssen (1999) is used the maximum increment in the spectrum, $|\Delta E|_{\max}$. The dissipation source function has been reformulated in terms of a mean steepness parameter and a mean frequency that gives more emphasis on the high-frequency part of the spectrum and results in a more realistic interaction between wind sea and swell (Bidlot et al., 2005). The bottom friction dissipation is modeled by the JONSWAP formulation (Hasselmann et al. (1973)) and the depth-induced breaking is based on the Battjes and Janssen (1979). More details of these parameterizations also can be found in Komen et al. (1994) and WAMDI Group (1988). The momentum transfer from the atmosphere to the sea surface (wind input) follows the Janssen theory (Janssen, 1991) allowing some dependence of the transfer from roughness length of the sea surface given by the sea state. The nonlinear interactions between the four wave–wave interactions are parameterized by the DIA-discrete interaction approximation (Hasselmann et al., 1985; Komen et al., 1994) in WAM.

3.1. Computation of extreme wave parameters

The deviations from normality are measured in terms of the kurtosis C_4 of the surface elevation probability density function in this version (Cy38r1) of the WAM model (ECMWF, 2012). With η the surface elevation the definition of kurtosis is:

$$C_4 = \frac{\langle \eta^4 \rangle}{\langle \eta^2 \rangle^2} - 1$$

According to the theory of wave–wave interactions the kurtosis is related to the frequency spectrum $E(\omega,\theta)$ by

$$C_4 = \frac{4g}{m_0^2} P \int d\omega_1 d\omega_2 d\omega_3 d\theta_1 d\theta_2 d\theta_3 T_{1,2,3,4} \sqrt{\frac{\omega_4}{\omega_1\omega_2\omega_3}} \frac{E_1E_2E_3}{\Delta\omega}$$

where P denotes the principle value of the integral and $\Delta\omega = \omega_1 + \omega_2 - \omega_3 - \omega_4$, and $T_{1,2,3,4}$ is a complicated, homogeneous function of the four wave numbers $\mathbf{k}_1$, $\mathbf{k}_2$, $\mathbf{k}_3$, $\mathbf{k}_4 = \mathbf{k}_1 + \mathbf{k}_2 - \mathbf{k}_3$. In addition, the angular frequency $\omega(\mathbf{k})$ obeys the dispersion relation $\omega(\mathbf{k}) = g\mathbf{k}$, with k the magnitude of the wavenumber vector $\mathbf{k}$.

Mori and Onorato found a fit for the maximum of the kurtosis (based on results from numerical simulations of the Nonlinear Schrödinger equation), which follows from the narrow-band limit of the Zakharov equation,

$$C_4^{dyn} = \frac{0.031}{\delta_\theta} x \frac{\pi}{3\sqrt{3}} \mathrm{BFI}^2$$

where BFI is the Benjamin–Feir index which is given by,

$$\mathrm{BFI} = \frac{\varepsilon\sqrt{2}}{\delta_\omega}$$

where $\varepsilon = k_0\sqrt{m_0}$ the integral steepness parameter, k_0 is the peak wave number, m_0 the spectral zero moment and δ_ω is the relative width of the frequency spectrum. The BFI is the ratio between nonlinearity and dispersion; its relation to the kurtosis has been found in the limit of large times and narrowband spectra neglecting directional spreading (Janssen, 2003).

Including the contribution from the shape of the waves, the total kurtosis becomes,

$$C_4 = C_4^{dyn} + \alpha\varepsilon^2$$

3.2. The wave model set up

The present configuration of WAM grid model covers almost the whole North Atlantic Ocean extended from (18°N, 80° N, 90°W, 30°E) at spatial resolution of 0.25°. The bathymetry grid data comes from the GEODAS NOAA's National Geophysical Data Centre (NGDC), with a resolution of 1 min of degree in latitude and longitude, which was linearly interpolated spatially to the 0.25° model grid.

In this WAM model configuration the wave spectrum is provided for 36 directional bands measured clockwise with respect to true north, and 30 frequencies logarithmically spaced from the minimum frequency of 0.0350 Hz up to 0.5552 Hz at intervals of $Df/f = 0.1$. JONSWAP spectrum at every grid point was set as initial condition with the following parameters: Phillips' parameters 0.18; peak frequency 0.2 Hz; overshoot factor 3.0; left peak width 0.07; right peak width 0.09; wave direction 0°; fetch 30,000 m.

The simulations began at 15th January 2007 (15 days before 1st February) to avoid any influence of the initial conditions on the study period from 1st–15th February 2007. CFSR wind fields have been linearly interpolated in space to 0.25° to match with the spatial resolution of the WAM model mesh. The wave hindcast temporal resolution was set to 1 h wind input/output time step. More details about the WAM configuration can be found in Table 1.

4. Dual extratropical cyclones

In February 2007, extreme Hs peak values were observed associated with two very intense extratropical cyclones (Cardone et al., 2011). The dual cyclones were highlighted in the Mariners Weather Log review of North Atlantic Ocean storms (Bancroft, 2007); wind speeds equivalent to category 3 hurricane scale were measured by QuikScat. In addition, the altimetry Hs peak value of 20.24 m on 10th February at 11:08 UTC was estimated from GFO satellite Ku-band altimeter at latitude at 48.14°N and 32.65°W The Hs peak value was associated to the second of the two extratropical cyclones. A detailed description based on the QuikScat wind speed data can be found in Cardone et al. (2011). The dual winter cyclones according to CFSR wind field are depicted in Fig. 2 (left) and although in the WAM Hs map (right) for 9th February 2007 at 12 UTC.

5. Validation of the WAM hindcast

The assessment of the WAM hindcast (Hs) is composed of three parts: (1) validation of WAM against a satellite orbit segment

Table 1
Numerical parameters for the WAM model configuration.

Parameter	Coarse grid
Integration time step	160 s
Spatial resolution	0.25°(27.8 km)
Number of points (x,y)	(481,249)
Propagation	Spherical
Frequencies	30
Directional bands	36
Frequency domain	0.0350–0.5552 Hz
Latitudes (°N)	18°; 80°
Longitudes (°W)	90°
Longitudes (°E)	30°
Type of model	Deep water
Wind input time step	1 h
WAM output time step	1 h
NCEP CFSR wind field spatial resolution	0.31°

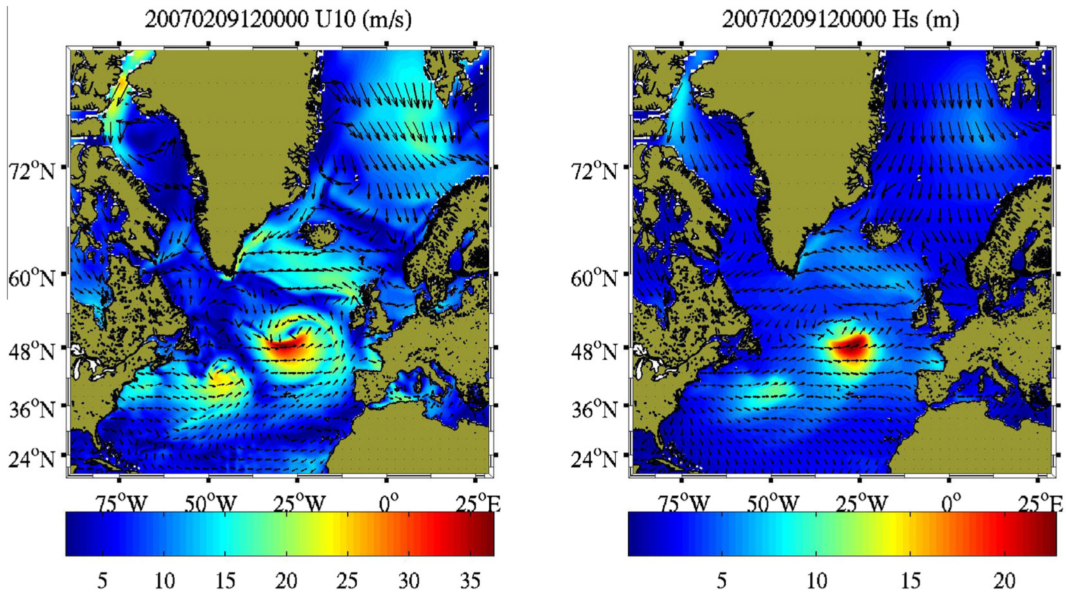

Fig. 2. High resolution CFSR wind field (left) and the WAM Hs map. Date: 9th February 2007 at 12 UTC (1st cyclone).

during the Hs extreme value; (2) comparison through scatter plots (WAM and JASON1) and (3). Comparison of WAM time series against wave buoys records and other databases.

Satellite data has the advantage of a great coverage over extended distances around the North Atlantic Ocean and the WAM results have been validated against the altimetry data measurements from JASON1 (Fig. 3) orbit segment coincident with the extreme sea state conditions of 9th February 2007 at 21:40 UTC. This particular segment of JASON1 data was previously analyzed by Cardone et al. (2009) that concluded on its reliability based on media filtering and cross-referencing with coincident meteorological data. From the comparison (Fig. 3) it can be seen that WAM compared well to the altimetry data along this orbit segment.

For validation purposes some statistical parameters were considered. The bias was defined as the difference between the mean observation and the mean prediction. The scatter index (s.i.) was defined as the standard deviation of the predicted data with respect to the best fit line, divided by the mean observations. The scatter plots for the Hs between WAM and JASON1 data (Fig. 4) for the period 1st–14th February 2007 shows the Hs higher than 20 m, a low scatter index of about 0.18, the best fit line slope of 1.05 and a correlation coefficient about 0.95 for a total number of records of 50,302.

The WAM hindcast (WAM-EC) was validated against two wave buoys: 62081 (lat.: 51°N; long.: 13.36°W, B1 in Fig. 1) and 62029 (lat.: 48.70°N; long.: 12.50°W, B2 in Fig. 1). Statistics between WAM-EC (blue dashed line) and buoys records (red line) (Fig. 5)

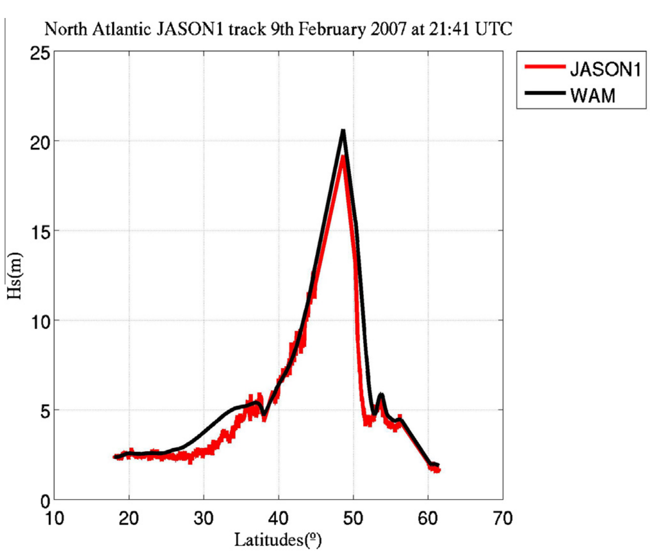

Fig. 3. Comparison of the WAM Hs against JASON1 Hs measured data along an orbit segment in an extreme sea state condition.

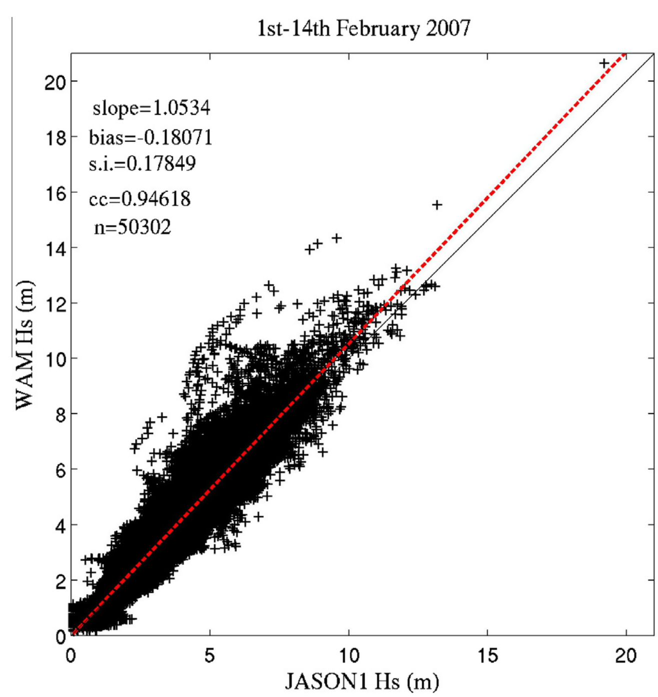

Fig. 4. Scatter plots of JASON1 observed Hs against WAM values. Period: 1st–14th February 2007. *n*-Number of records; cc-correlation coefficient; s.i.-scatter index.

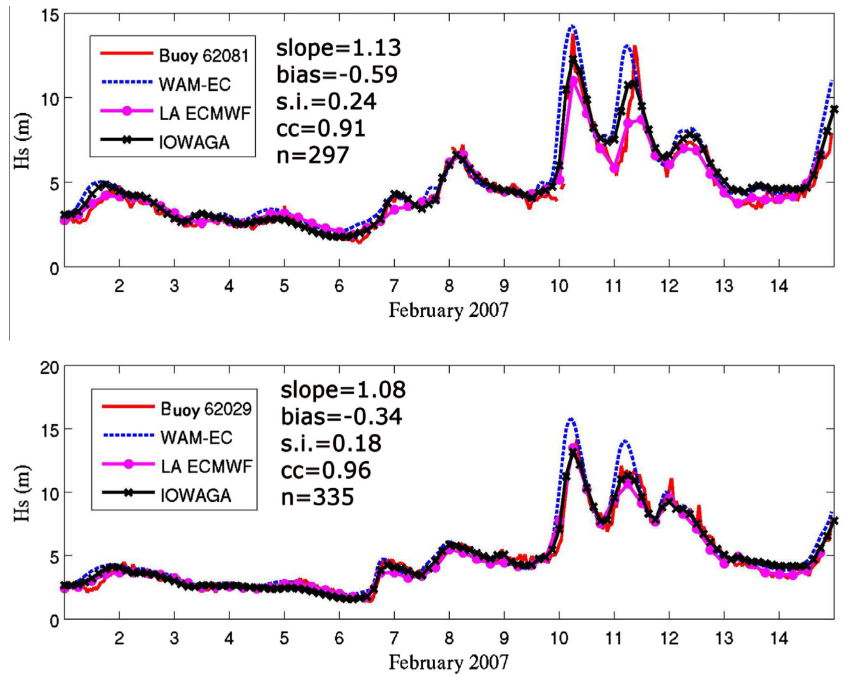

Fig. 5. Time series for the Hs: WAM-EC (blue dashed line), buoy 62029 (solid red line); IOWAGA (black line) and LA ECMWF (magenta line). The statistical parameters shown correspond to the WAM-EC against buoy record at every 1 h. (For interpretation of the references to colour in this figure legend, the reader is referred to the web version of this article.)

show that in general a good agreement was obtained. From the time series the best fit line scatter indexes are 0.24 (top panel) and 0.18 (bottom panel). In terms of the best fit line slope and correlation coefficient (cc) the best correlation corresponded to buoy 62029 (bottom panel) with 1.08 and 0.96, respectively. However, in both locations WAM-EC model overestimated the computed Hs as can be seen (bias = −0.59 (top); bias = −0.34 (bottom).

Additionally, the WAM hindcast (Hs) was compared against two well known databases: IOWAGA (Rascle and Ardhuin, 2013) and ECMWF limited area model (LA ECMWF) (Dee et al., 2011; ECMWF, 2012). On the case of the buoy 62081 (Fig. 5, top panel) a time shift was observed during the second storm for the IOWAGA and WAM-EC hindcasts.

On the case of the buoy 62029 (Fig. 5, bottom panel) the WAM-EC hindcast overestimated the Hs peaks. Otherwise, the WAM-EC results (blue dashed line) are comparable to the results of the two databases.

6. Results and discussions

6.1. Spatial distribution of extreme wave parameters in the North Atlantic

In this section first the spatial distribution at the 9th February is described from a general point of view in the whole the numerical simulation domain and secondly, the focus is on the distribution of BFI, kurtosis and the ratio of maximum wave height and Hs.

As shown in Section 4, the winter cyclones (Fig. 2) exhibit wind speeds higher than 35 m/s and for the case of the first cyclone (the more intense) the Hs values are higher than 20 m. In association with these realistic conditions obtained from the hindcast for 9th February 12 UTC, the spatial distribution of the BFI (Fig. 6, left panel) for the same date shows maxima values in first and fourth quadrants of the 1st and 2nd cyclones, respectively. The BFI reaches values around 1.5 for the 1st cyclone and on the case of the second one was about 0.7. For the first cyclone the BFI maxima are located in the 1st and 4th quadrants indicating that at these places are more prone to abnormal waves than others (quadrant's definition can be found in Fig. 8). Kurtosis shows similar spatial distribution as BFI with maxima values (3.15) in first and fourth quadrants (Fig. 6, right panel).

6.2. Spatial–temporal distribution of extreme wave parameters around the eye of cyclones

In order to study the temporal–spatial distributions of the main abnormal wave's parameters the analysis was focused on high occurrence of very extreme sea states region (Cardone et al., 2011) with geographical limits: 62°N, 42°N, 40°W, 22°W and hereafter VESS region. The results from the WAM hindcast are mainly discussed for 9th and 10th February 2007, dates during which were observed the extreme wave height values.

Time series of wind speed (U_{10}), Hs, BFI, kurtosis (C_4), directional spreading (σ_θ) and peak period (Tp) from the hindcast from the 1st to the 14th of February are shown in Fig. 7 for three locations in the VESS region around the cyclones at P1, P2 and P3 (Fig. 1). The CFSR reanalysis wind speed (U_{10}) time series shows clearly the two U_{10} maxima (Fig. 7 first panel), higher than 35 m/s, at P2 and P3 (Fig. 1) associated with the two winter cyclones that crossed the region between the 9th and 11th of February. The significant wave height (Hs) (second panel) exhibits two maxima higher than 20 m associated with the passage of the extratropical cyclones. There is a lag of few hours between the maxima of U_{10} and Hs at P2 and P3 for both cyclones. This is due to the relative position of both points with respect to the cyclone tracks. At both locations, however, the Hs attains the maxima values at the same time as the 10 m wind speed. Both P2 and P3 are located south of the cyclones tracks so that observing the directions of propagation of both cyclones, these points are always located to the right of the tracks (in the 1st and 4th quadrants) where the U_{10} and Hs are higher than in the other quadrants. Location P1 is, on the other

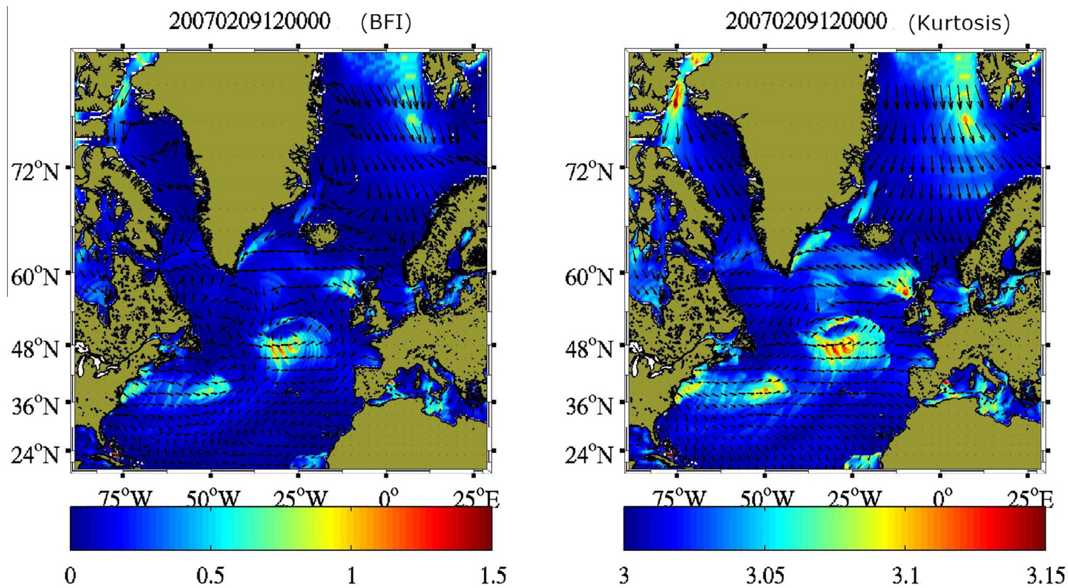

Fig. 6. BFI (left) and the kurtosis (right) spatial distribution. Date: 9th February 2007 at 12 UTC.

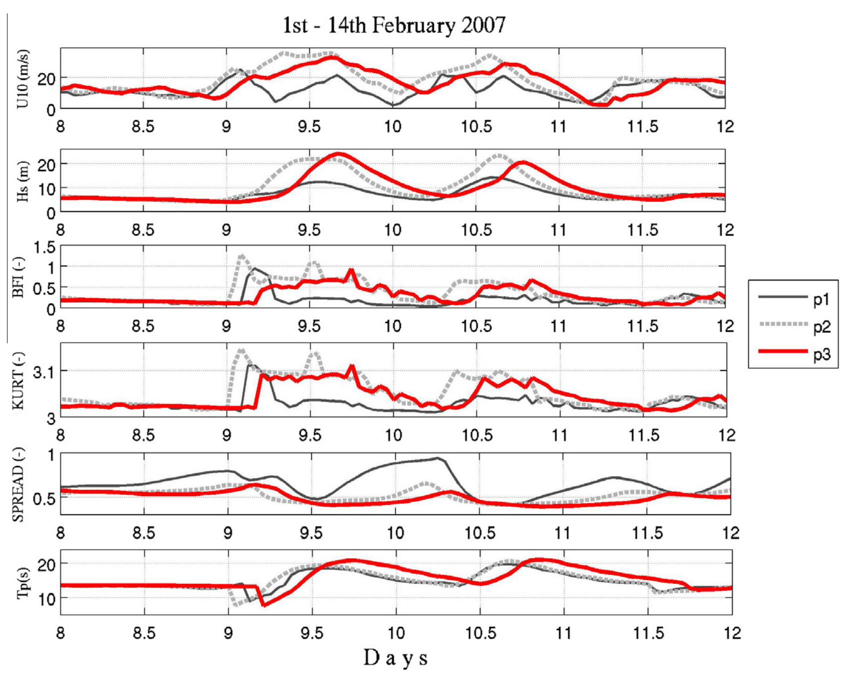

Fig. 7. CFSR wind speed (U_{10}) time series (top); WAM time series: significant wave height (Hs) (second panel), Benjamin–Feir index (BFI) (3rd panel), kurtosis (KURT) (4th panel), directional spreading (SPREAD) (5th panel) and the peak period (Tp) at P1, P2 and P3 for 8th–12th February 2007.

hand, located to the left of the track for the first cyclone, resulting in lower U_{10} and Hs relative to P2 and P3.

The temporal evolution of the BFI shows that during the cyclone passage in the VESS region this parameter attains two maxima above 1.0 at P2 (Fig. 7 Third panel) and one maximum close to 1.0 at P3 and at P1. The first BFI maximum at P2 occurs without a corresponding Hs maximum, which lags behind a few hours: the highest BFI was obtained at P2 with 1.25 the 9th February at 01 UTC, while the Hs maximum occurs at the 9th February at 12 UTC. The BFI maximum (higher than 1) is associated with the fact that P2 is nearby to the eye on 9th at 06 UTC. The secondary maxima of BFI ($\sim$1) occurred simultaneously with the Hs maximum at P2 and at P3 the BFI and Hs maxima occurs simultaneously. At P1, the BFI maximum occurs without a significant increase in the Hs. As background to these maxima, the BFI time series show an increase during the passage of the two cyclones, with the first cyclone causing slightly higher increases (Fig. 7). The kurtosis time series (fourth panel) shows a similar evolution as the BFI time series. The directional spreading time series presents relatively low values during the cyclone passage at P2 and P3 while at P1 there

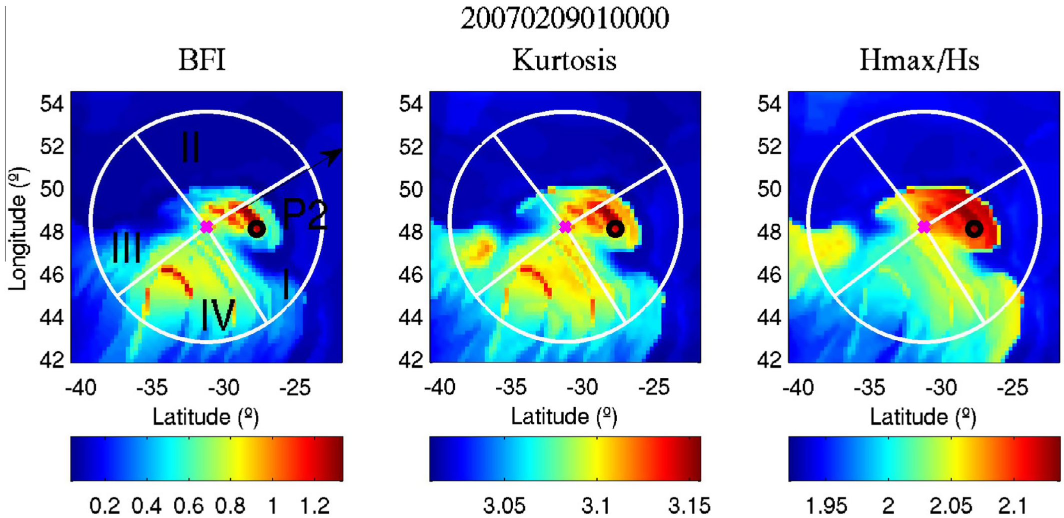

Fig. 8. Distribution of BFI, kurtosis and Hmax/Hs. Date: 9th February, 01 UTC. Black arrow-cyclone propagation direction; black circle-P2.

is a pronounced increase in directional spreading around the 10th of February at 00 UTC. Maxima of Tp during the cyclone passage are higher than 20 s at P2 and P3 and coincide generally with Hs maxima. It was observed a sudden decrease of Tp coinciding with the steep increase of the BFI around the 9th of February at 00 UTC.

At location P2 the BFI reaches its maximum values during the passage of the two cyclones. For the first cyclone these maxima are greater than 1 at the 9th of February at 01 UTC and at 12 UTC. In Fig. 8, the spatial distributions of the BFI parameter, kurtosis and the abnormality index (Hmax/Hs) are shown for 9th of February at 01 UTC in a region with ~1400 km side centred at the cyclone centre. The BFI distribution shows two regions with higher values: the 4th quadrant and a lobe shaped region in front of the cyclone centre (1st and 2nd quadrants) mainly located in the 1st quadrant. The 2nd and 3rd quadrant are practically devoid of high BFI values. At this date the P2 location is located in the 1st quadrant inside the lobe region. The high BFI values at the 4th quadrant may be due to the steepness ($k_p\sqrt{m_0}$) of the waves (Mori, 2012) because in this area occurs the maximum Hs, were U_{10} is high (Fig. 9, top panels). However, the highest U_{10} are found to the northwest (towards the 3rd quadrant) from the Hs maximum. This difference could be due to the diminishing wind speed towards the Hs maximum balanced by the smaller difference between wind and dominant wave direction found towards the Hs maximum also

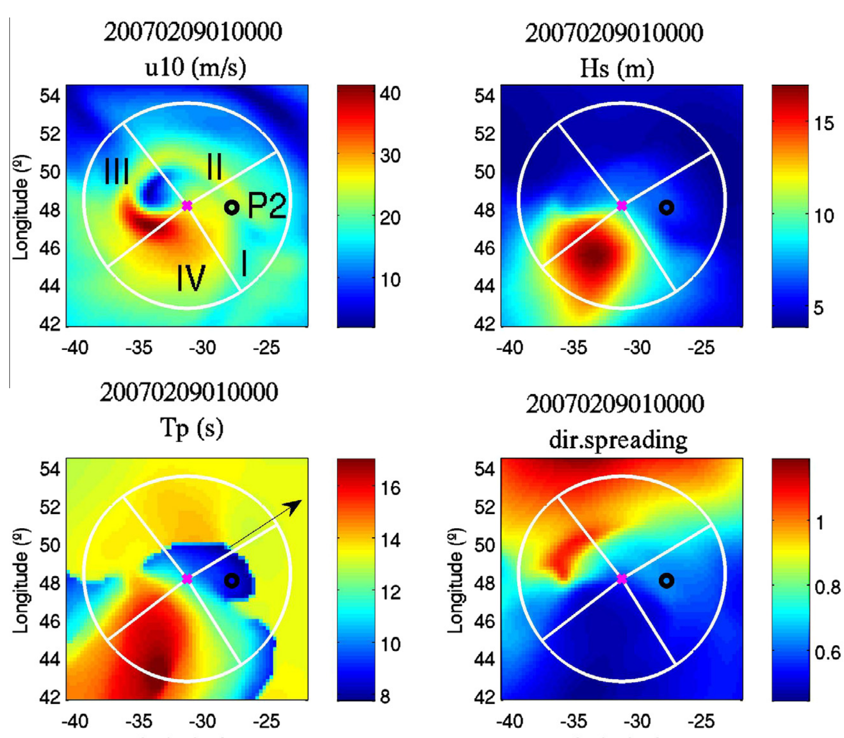

Fig. 9. Distribution of the wind speed (U_{10}), Hs, peak period (Tp) and directional spreading around the cyclone eye. I, II, III, IV-number of quadrants. Date: 9th February, 01 UTC. Black arrow-cyclone propagation direction; black circle-P2.

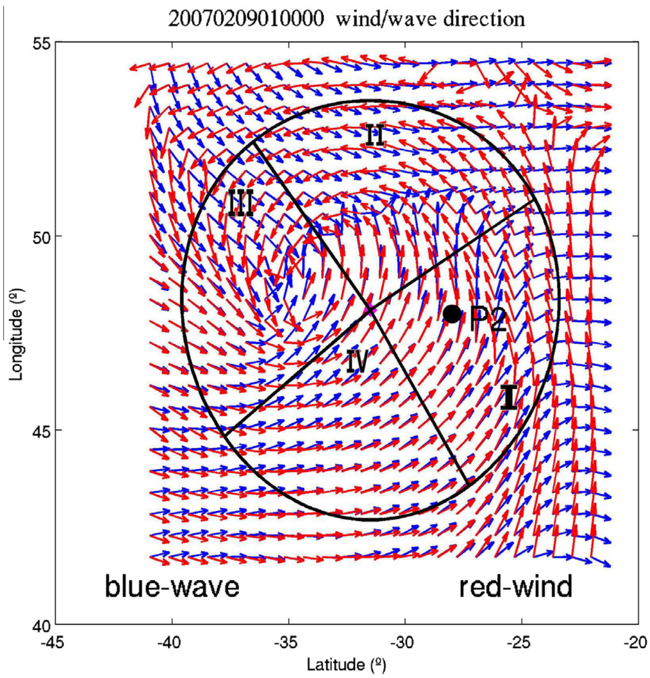

Fig. 10. Wind and wave directions around the eye of the first cyclone. Date: 9th February at 01 UTC. I, II, III, IV-number of quadrants. black point-P2.

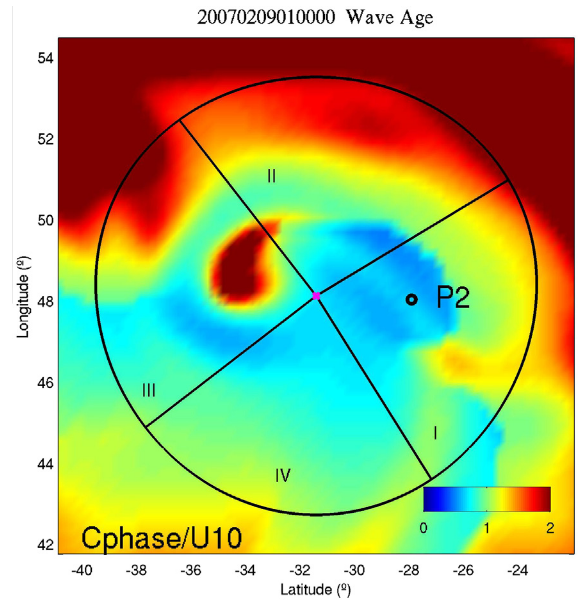

Fig. 11. Wave age around the eye of the first cyclone. Date: 9th February, 01 UTC.

(Fig. 10). At P2, however, the Hs values are relatively small, but the peak wave number is higher than in the 4th quadrant so the waves are steep also in the lobe region. The lobe region corresponds to a region with low peak period of the order of 8 s (Fig. 9, bottom left panel), whose limits follow very closely the limits of the high BFI region. The exception to this is the 4th quadrant where there are large Tp and large BFI, mainly due to large Hs. The directional spreading (Fig. 9, bottom right panel), a factor that suppresses non-linear enhancement of sea states is low (<0.8) in the 1st and 4th quadrants especially where the wind direction and wave direction do not show large differences. In this region young waves with $c_p/U_{10} < 1$ (Fig. 11) can be found up to mature wind-sea (Young, 2006). In most of the 2nd and 3rd quadrants, conditions for abnormal wave occurrence seem to be absent. Small Hs and high Tp do not favor the existence of steep waves and the directional spreading is large, suppressing nonlinear enhancement of the sea state. The distribution of the abnormality index Hmax/Hs (Fig. 8, right panel) shows the highest values in the lobe region. This is probably due to two different factors: firstly, the kurtosis is high in this region, but also the number of waves (N) is also high due to the small Tp that is found there. The influence of the number of waves on the Hmax distribution can be seen by observing that the regions of low Tp (high N, for the same storm duration) have also high Hmax/Hs although the kurtosis is lower there than in the 4th quadrant, where Hmax/Hs is generally lower than in those regions mentioned above and where kurtosis attains higher values.

The second BFI maximum is attained at P2 on the 9th February 12 UTC. The distribution of BFI, C_4 and Hmax/Hs are shown for this date in Fig. 12. The P2 location is now in the 4th quadrant, where

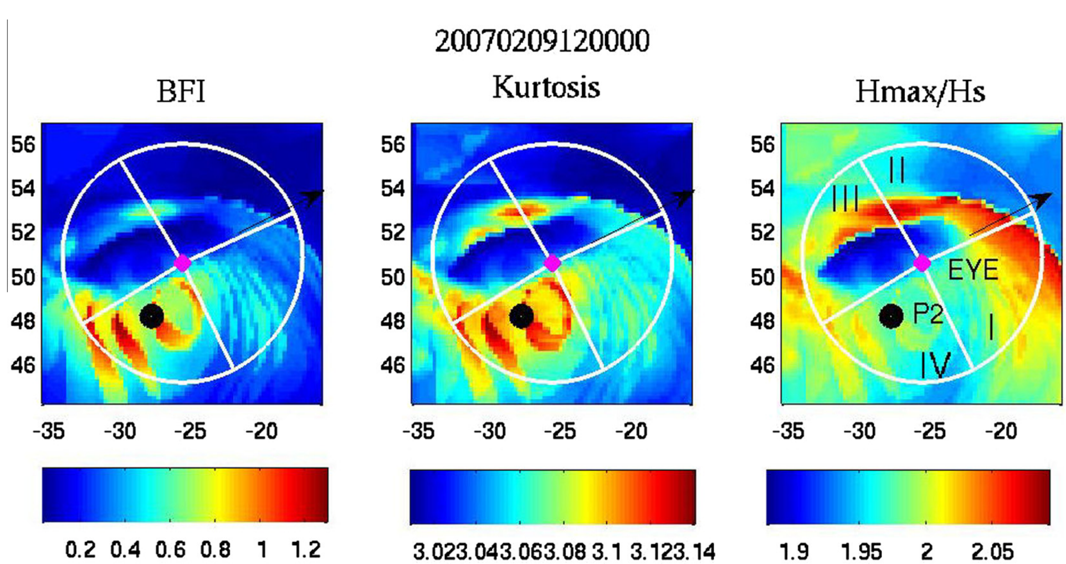

Fig. 12. Freak parameters distribution BFI, Kurtosis and Hmax/Hs. Date: 9th February, 12 UTC. Black arrow-cyclone direction of propagation; black circle-P2.

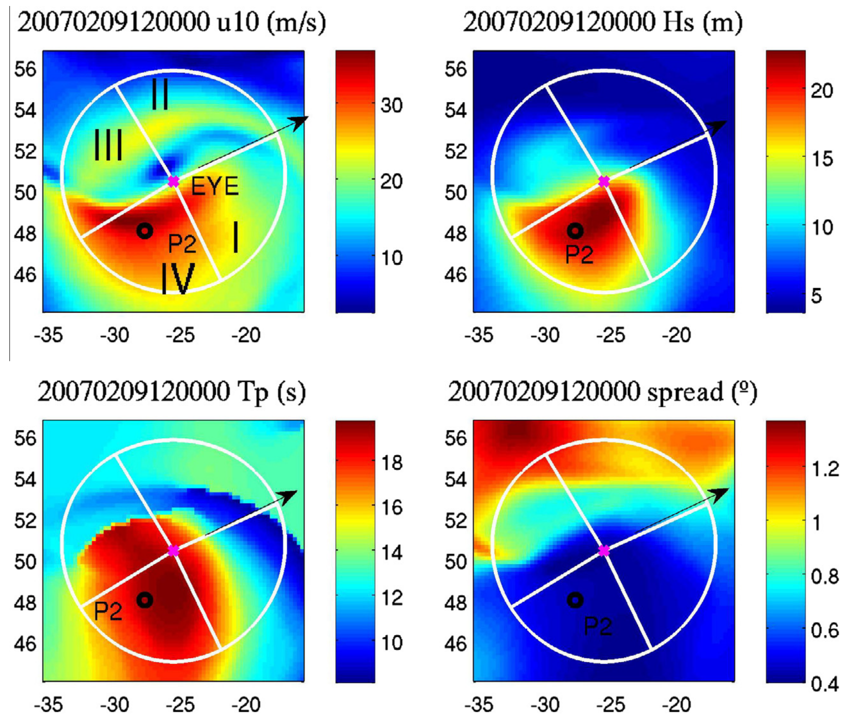

Fig. 13. Distribution of wind speed (U_{10}), Hs, peak period (Tp) and directional spreading around the cyclone eye. I, II, III, IV-number of quadrants. Date: 9th February, 12 UTC.

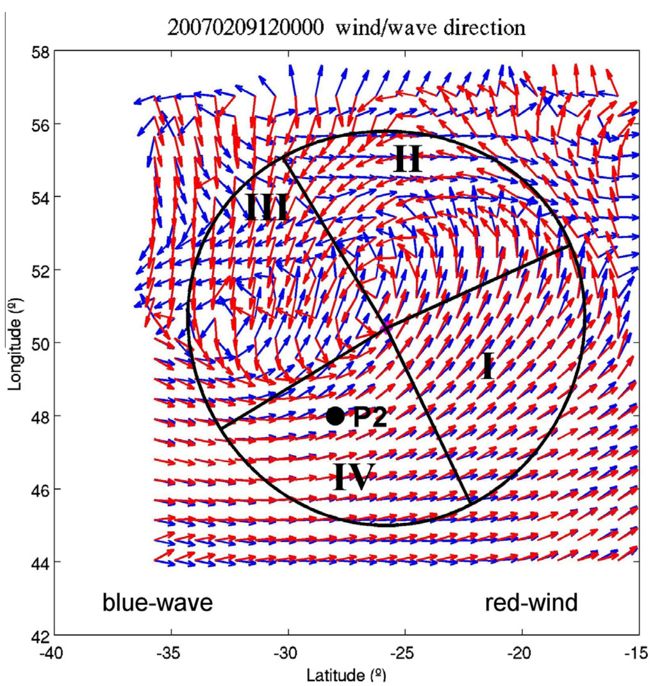

Fig. 14. Wind and wave directions around the eye of the first cyclone. Date: 9th February at 12 UTC. I, II, III, IV-number of quadrants. black point-P2.

the high BFI values can be found (left panel). The C_4 distribution (middle panel) follows closely the BFI values. The 4th quadrant is the region where the highest U_{10} and Hs (Fig. 13, top left and right panels) can be found and also the lowest σ_θ. In this quadrant, the wind and wave direction almost coincide (Fig. 14), and this also occurs in the 1st quadrant, where σ_θ is also low. The Hmax/Hs criterion (Fig. 12, right panel) shows also a strong relationship to Tp, visible in the strip of low Tp and high Hmax/Hs that crosses the 1st and 2nd quadrants of the cyclone.

7. Concluding remarks

North Atlantic extratropical cyclones can generate sea states with expected wave heights of the order of 20 m. But also abnormal waves may occur which double the expected wave height. In the present study for a realistic hindcast of the extratropical cyclones in the North Atlantic the results show that the large significant wave height occurs in the 4th quadrant where the winds are stronger (Figs. 9 and 13). The chance of abnormal wave occurrence is also high in this quadrant. However, abnormal waves can occur also in regions of the cyclone where the winds are relatively weak, as long as the wind direction and the wave direction are close (Figs. 10 and 14). In this region young waves with $c_p/U_{10} < 1$ (Fig. 11) can be found up to mature wind–sea. From the results obtained it can be seen that the directional spread reduces the nonlinear enhancement of the sea state when the wind and wave directions are not aligned. The Hmax to Hs ratio (abnormality index) is maximum not only within areas were kurtosis is high but also in the areas where young waves with low Tp are present because the number of waves increases.

A forecast system that can be predict the time and locations of high probability of rogue waves in the North Atlantic, incorporating that in a warning system, is an important tool to be used in risk minimization and accident prevention due to rogue wave impacts on ships and platforms. The obtained results are relevant for the operational wave forecasts, maritime navigation and consequently for the ship safety in extreme seas since it shows that in the areas of the ocean around the eye of the cyclones, where the wind and wave directions are similar the probability of occurrence of abnormal waves is enhanced.

Acknowledgements

The authors are thankful to Dr. Jean Bidlot (ECMWF) who supplied the WAM outputs from the ECMWF limited area model. This work has been performed within the project CLIBECO- Present and future marine climate in the Iberian coast, funded by the Portuguese Foundation for Science and Technology (FCT- Fundação Portuguesa para a Ciência e a Tecnologia) under contract n.°: EXPL/AAG-MAA/1001/2013. The first author has been financed by the Portuguese Foundation for Science and Technology (FCT-Fundação para a Ciência e Tecnologia) through grant SFRH/BPD/84358/2012.

References

Alkhalidi, M.A., 2012. Asymptotic wave-height distributions and conditional statistics. Kuwait Univ. J. Sci. Eng. 39 (1B), 79–92.
Alkhalidi, M.A., Tayfun, M.A., 2013. Generalized Boccotti distribution for nonlinear wave heights. Ocean Eng. 74, 101–106.
Ash, E., Busswell, G., Pinnock, S., 2012. DUE Globwave Wave Data Handbook. Logica, UK Ltd., pp. 74.
Bancroft, G.P., 2007. Marine weather review – North Atlantic area January through April, 2007. Mariners Weather Log 51, 38–53.
Battjes, J.A., Janssen, J.P.F.M., 1979. Energy loss and set-up due to breaking of random waves. In: Proceedings of 16th International Conference on Coastal Engineering, 569–587, Hamburg Germany.
Bidlot, J., Janssen, P.A.E.M., Abdalla, S., 2005. A revised formulation for ocean wave dissipation in CY29R1. Memorandum Research Department, ECMWF, April 7, 2005 File: R60.9/JB/0516.
Bidlot, J., 2012. Intercomparison of operational wave forecasting systems against buoys: data from ECMWF, MetOffice, FNMOC, MSC, NCEP, MeteoFrance, DWD, BoM, SHOM, JMA, KMA, Puerto del Estado, DMI, CNR-AM, METNO, SHN-SM. August 2012–October 2012. European Centre for Medium-range Weather Forecasts. November 25, 2012.
Boccotti, P., 1981. On the highest waves in a stationary Gaussian process. Atti de lla Accademia Ligure di Scienzee Letter 38, 271–302.
Boccotti, P., 1989. On mechanics of irregular gravity waves. Atti Accad. Naz. Lincei 5, 111–170.
Boccotti, P., 2000. Wave Mechanics for Ocean Engineering. Elsevier Science, Amsterdam.
Cardone, V.J., Cox, A.T., Morrone, M.A., Swail, V.R., 2009. Satellite altimeter detection of global extreme sea states. In: 11th International Workshop on Wave Hindcasting and Forecasting, Halifax N.S., October 18–23, 2009.
Cardone, V.J., Cox, A.T., Morrone, M.A., Swail, V.R., 2011. Global distribution and associated synoptic climatology of very extreme sea states (VESS). In: Proceedings 12th International Workshop on Wave Hindcasting and Forecasting, Hawaii, October 31–November 4.
Casas-Prat, M., Holthuijsen, L.H., 2010. Short-term statistics of waves observed in deep water. J. Geophys. Res. 115, 5742–5761.
Chawla, A., Spindler, D.M., Tolman, H.L., 2013. Validation of a thirty year wave hindcast using the climate forecast system reanalysis winds. Ocean Model. 70, 189–206.
Cherneva, Z., Tayfun, M.A., Guedes, Soares C., 2009. Statistics of nonlinear waves generated in an offshore wave basin. J. Geophys. Res. 114, C08005. http://dx.doi.org/10.1029/2009JC005332.
Dee, D.P., Uppala, S.M., Simmons, A.J., Berrisford, P., Pol, P., Kobayashi, S., Andrae, U., Balmaseda, M.A., Balsamo, G., Bauer, P., Bechtold, P., Beljaars, A.C.M., van de Berg, L., Bidlot, J., Bormann, N., Delsol, C., Dragani, R., Fuentes, M., Geer, A.J., Haimberger, L., Healy, S.B., Hersbach, H., Hólm, E.V., Isaksen, L., Kallberg, P., Kohler, M., Matricardi, M., McNall, A.P., Monge-Sanz, B.M., Morcrette, J.J., Park, B.K., Peubey, C., de Rosnay, P., Tavolato, C., Thepaut, J.N., Vitart, F., 2011. The ERA-interim reanalysis: configuration and performance of the data assimilation system. Q. J. R. Meteorol. Soc. 137, 553–597. http://dx.doi.org/10.1002/qj.828.
Dean, R., 1990. Abnormal waves: a possible explanation. In: Torum, A., Gudmestat, O. (Eds.), Water Wave Kinematics. Kluwer, pp. 609–612.
Durrant, T.H., Greenslade, D.J.M., Simmonds, I., 2009. Validation of Jason-1 and Envisat remotely sensed wave heights. J. Atmos. Oceanic Technol. 26, 123–134.
ECMWF, 2012. Wave model. Part VII: IFS Documentation – Cy38r1. Operational implementation, Part VII: ECMWF wave model, pp. 79.
Faulkner, D., Buckley, W.H., 1997. Critical survival conditions for ship design. In: International Conference on Design and Operation for Abnormal Conditions, RINA, UK, paper No. 6, pp. 1–25.
Forristall, G.Z., 1984. The distribution of measured and simulated wave heights as a function of spectral shape. J. Geophys. Res. 89, 547–552.
Gramstad, O., Trulsen, K., 2007. Influence of crest and group length on the occurrence of freak waves. J. Fluid Mech. 582, 463–472.
Goda, Y., 2000. Random Seas and Design of Maritime Structures. World Scientific, New Jersey.
Guedes, Soares C., Cherneva, Z., Antao, E., 2003. Characteristics of abnormal waves in North Sea storm seas. Appl. Ocean Res. 25, 337–344.
Guedes, Soares C., Cherneva, Z., Antao, E., 2004. Abnormal waves during hurricane Camille. J. Geophys. Res. 109, C08008. http://dx.doi.org/10.1029/2003JC002244.
Guedes, Soares C., Fonseca, N., Pascoal, R., 2008. Abnormal wave induced load effects in ship structures. J. Ship Res. 52 (1), 30–44.
Guedes Soares, C., Cherneva, Z., Petrova, P.G., Antao, E., 2011. Large waves in sea states. In: Guedes Soares, C., Garbatov, Y., Fonseca, N., Teixeira, A.P. (Eds.), Marine Technology and Engineering. Taylor & Francis Group, London, UK, pp. 79–95.
Hasselmann, K., Barnett, T.P., Bouws, E., Carlson, H., Cartwright, D.E., Enke, K., Ewing, J.A., Gienapp, H., Hasselmann, D.E., Kruseman, P., Meerburg, A., Müller, P., Olbers, D.J., Richter, K., Sell, W., Walden, H., 1973. Measurements of wind-wave growth and swell decay during the joint North Sea wave project (JONSWAP). Dtsch. Hydrogr. Z. Suppl. A 8 (12), 95.
Hasselmann, S.K., Hasselmann, J., Allender, H., Barnett, T.P., 1985. Computations and parameterizations of the nonlinear transfer in a gravity-wave spectrum. Part I: a new method for efficient computations of the exact nonlinear transfer integral. J. Phys. Oceanogr. 15, 1369–1377.
Hersbach, H., Janssen, P.A.E.M., 1999. Improvements of the short fetch behaviour in the WAM model. J. Atmos. Oceanic Technol. 16, 884–892.
Janssen, P.A.E.M., 1991. Quasi-linear theory of wind-wave generation applied to wave forecasting. J. Phys. Oceanogr. 21, 1631–1642.
Janssen, P.A.E.M., 2003. Nonlinear four-wave interactions and freak waves. J. Phys. Oceanogr. 33 (4), 863–884.
Janssen, P.A.E.M., Bidlot, J.R., 2009. On the extension of the freak wave warning system and its verification. Issue 588 of ECMWF technical memorandum, pp. 42.
Kharif, C., Pelinovsky, E., 2003. Physical mechanisms of the rogue wave phenomenon. Eur. J. Mech. B/Fluids 22, 603–634.
Kharif, C., Pelinovsky, E., Slunyaev, A., 2008. Rogue Waves in the Ocean. Springer, Berlin, 216 pp.
Komen, G.J., Cavaleri, L., Donelan, M., Hasselmann, K., Hasselmann, S., Janssen, P.A.E.M., 1994. Dynamics and Modelling of Ocean Waves. Cambridge University Press.
Lavrenov, I., 1998. The wave energy concentration at the Agulhas current off South Africa. Nat. Hazard 17, 117–127.
Longuet-Higgins, M.S., 1952. On the statistical distribution of the heights of the sea waves. J. Mar. Res. 11 (3), 245–266.
Longuet-Higgins, M.S., Cartwright, D.E., Smith, N.D., 1963. Observations of the directional spectrum of sea waves using the motions of a floating buoy. In: Ocean Wave Spectra. Prentice Hall, Upper Saddle River, N. J, pp. 111–136.
Longuet-Higgins, M.S., 1980. On the distribution of the heights of sea waves: some effects of nonlinearity and finite bandwidth. J. Geophys. Res. 85, 1519–1523.
Mori, N., Janssen, P.A.E.M., 2006. On kurtosis and occurrence probability of freak waves. J. Phys. Oceanogr. 36 (7), 1471–1483.
Mori, N., Onorato, M., Janssen, P.A.E.M., 2011. On the estimation of the kurtosis in directional sea states for freak wave forecasting. J. Phys. Oceanogr. 41 (8), 1484–1497.
Mori, N., 2012. Freak waves under typhoon conditions. J. Geophys. Res. 117, C00J07. http://dx.doi.org/10.1029/2011JC007788.
Onorato, M., Osborne, A.R., Serio, M., Cavaleri, L., Brandini, C., Stansberg, C.T., 2004. Observation of strongly non-Gaussian statistics for random sea surface gravity waves in wave flume experiments. Phys. Rev. 70, 067302.
Onorato, M., Cavaleri, L., Fouques, S., Gramstad, O., Janssen, P.A.E.M., Monbaliu, J., Osborne, A.R., Pakozdi, C., Serio, M., Stansberg, C.T., Toffoli, A., Trulsen, K., 2009. Statistical properties of mechanically generated surface gravity waves: a laboratory experiment in a three-dimensional wave basin. J. Fluid Mech. 627, 235–257. http://dx.doi.org/10.1017/S002211200900603X.
Petrova, P.G., Guedes, Soares C., 2011. Wave height distributions in bimodal sea states from offshore basins. Ocean Eng. 38 (4), 658–672.
Queffeulou, P., Croize-Fillon, D., 2012. Global altimeter SWH data set. Version 9, April, Technical Report, IFREMER.
Rascle, N., Ardhuin, F., 2013. A global wave parameter database for geophysical applications. Part 2: model validation with improved source term parameterization. Ocean Model. 70, 174–188.
Saha Suranjana, S., Moorthi Pan, H.L., Wu, X., Wang, J., Nadiga, S., Tripp, P., Kistler, R., Wooll, J., Behringer, D., Liu, H., Stokes, D., Grumbine, R., Gayno, G., Wang, J., Hou, Y.T., Chuang, H., Juang, H.M.H., Sela, J., Iredell, M., Treadon, R., Kleist, D., Van Dels, P., Keyser, D., Derber, J., Ek, M., Meng, J., Wei, H., Yang, R., Lord, S., van den Dool, H., Kumar, A., Wang, W., Long, C., Chelliah, M., Xue, Y., Huang, B., Schemm, J.K., Ebisuzaki, W., Lin, R., Xie, P., Chen, M., Zhou, S., Higgins, W., Zou, C., Liu, Q., Chen, Y., Han, Y., Cucurull, L., Reynolds, R.W., Rutledge, G., Goldberg, M., 2010. The NCEP climate forecast system reanalysis. Bull. Am. Meteor. Soc. 91, 1015–1057.
Serreze, M.C., Carse, F., Barry, R.G., Rogers, J.C., 1997. Icelandic low cyclone activity: climatological features, linkages with the NAO, and relationships with recent changes in the northern hemisphere circulation. J. Clim. 10, 453–464.
Serreze, M.C., Barrett, A.P., 2008. The summer cyclone maximum over the central Arctic ocean. J. Clim. 21, 1048–1065. http://dx.doi.org/10.1175/2007JCLI1810.1.
Serreze, M.C., 2009. Northern hemisphere cyclone locations and characteristics from NCEP/NCAR reanalysis data. Boulder, National snow and ice data center, Digital media, Colorado USA.
Tayfun, M.A., 1990. Distribution of large wave heights. J. Waterway Port Coastal Ocean Eng. 116, 686–707.
Tayfun, M.A., Fedele, F., 2007. Wave-height distributions and nonlinear effects. Ocean Eng. 34, 1631–1649.
Trulsen, K., Dysthe, K.B., 1997. Freak waves—a three-dimensional wave simulation. In: Proceedings of the Twenty-First Symposium on Naval Hydrodynamics, Natl. Acad. of Sci., Washington, D.C., pp. 550–558.
Veltcheva, A., Guedes, Soares C., 2012. Analysis of abnormal wave groups in hurricane Camille by the Hilbert Huang transform method. Ocean Eng. 42, 102–111.

WAMDI Group, 1988. The WAM model—a third generation ocean wave prediction model. Phys. Oceanogr. 18(12), pp. 1775–1810.
Waseda, T., 2006. Impact of directionality on the extreme wave occurrence in a discrete random wave system. In: Proceedings of 9th International Workshop on Wave Hindcasting and Forecasting, Victoria, Canada.
Yasuda, T., Mori, N., 1997. Occurrence properties of giant freak waves in sea area around Japan. J. Waterway Port Coastal Ocean Eng. 123 (4), 209–213.
Young, I.R., 2006. Directional spectra of hurricane wind waves. J. Geophys. Res. 111 (C08020), 1–14. http://dx.doi.org/10.1029/2006JC003540.